J Mater Sci: Mater Electron **(2025) 36:862**

$Ag/Ga_2O_3/n$-Si Schottky-type photodetector for visible light detection

Mehmet Yilmaz[1], Adem Kocyigit[2,*], Erman Erdogan[2], Murat Yıldırım[3], and Maria Luisa Grilli[4]

[1] *Department of Science Teaching, Education Faculty, Suleyman Demirel University, 32260 Isparta, Turkey*
[2] *Department of Electronics and Automation, Vocational High School, Bilecik Şeyh Edebali University, 11100 Bilecik, Turkey*
[3] *Department of Biotechnology, Faculty of Science, Selcuk University, 42130 Konya, Turkey*
[4] *Energy Technologies and Renewable Sources Department, ENEA-Italian National Agency for New Technologies, Energy and Sustainable Economic Development, Casaccia Research Centre, Via Anguillarese 301, 00123 Rome, Italy*

Received: 14 February 2025
Accepted: 26 April 2025
Published online: 23 May 2025

© The Author(s), 2025

ABSTRACT

Gallium oxide (Ga_2O_3) is an ultra-wide band gap material which has been receiving increasing interest for its potential applications in power electronics, ultraviolet (UV) photodetectors, and gas sensors. In this study, we have synthesized β-phase Ga_2O_3 on n-Si substrate using the electrodeposition technique, and investigated its properties for use in photodetector applications for broadband detection combining Si and Ga_2O_3. X-ray diffractometer (XRD), scanning electron microscope (SEM) with energy dispersive x-ray (EDX) analysis were conducted to illuminate structural and morphological behaviors of the Ga_2O_3. Ag metallic contacts on the Ga_2O_3/n-Si junction and Al ohmic contact on the back surface of the n-Si were obtained by thermal evaporation technique. Thus, $Ag/Ga_2O_3/n$-Si Schottky-type photodetectors were fabricated and characterized by current–voltage (*I-V*) measurements depending on various light power intensities and wavelengths ranging from UV to near-infrared (NIR). The diode characteristics, as well as the photodetection parameters such as responsivity, specific detectivity, and external quantum efficiency (*EQE*) were determined and discussed in detail. The $Ag/Ga_2O_3/n$-Si Schottky-type photodetectors showed high performances: 122.88 A/W responsivity, 1.07×10^{12} Jones specific detectivity, and very high *EQE* value of 2.18×10^4% at 700 nm wavelength. The obtained $Ag/Ga_2O_3/n$-Si Schottky-type photodetector exhibits promising potential as a candidate for optoelectronic applications in the visible range. These photodetectors can be used in visible light communication, light sensing and cameras.

Address correspondence to E-mail: adem.kocyigit@bilecik.edu.tr

https://doi.org/10.1007/s10854-025-14892-y

1 Introduction

The promising advantages of wide bandgap semiconductor oxides have pushed researchers to carry out investigations on the development of oxide semiconductor devices for practical applications [1]. In recent years, research on oxide materials has become very intensive due to the possibility of tailoring semiconducting oxides' properties by changing their nanostructures [2]. With the development of nanotechnology, oxide semiconductor materials have attracted great attention due to their application potential in field-effect transistors [3], lithium-ion batteries [4], UV photodetectors [5], and gas sensors [6].

There are many oxide semiconductor materials such as SnO_2, ZnO, TiO_2 etc. which are used in various applications of flexible electronics, displays, and smart technologies [7, 8]. Ga_2O_3 is one of the ultra-wideband gap oxide semiconductors, with band gap values between 4.7 and 4.9 eV, and can be employed in various technological applications. Ga_2O_3 shows six different crystal phases of α, β, γ, δ, κ, and ε, of which α and β phases are the stable ones [9]. The β phase is the most thermally and chemically stable among the crystal structures; the α phase has a much smaller band gap. For those reasons, studies on gallium oxide generally focus on the β phase. The resistivity of β-Ga_2O_3 can be changeable depending on fabrication temperature, doping level and atmospheric conditions due to its semiconducting behavior [10, 11]. Due to its chemical and thermal stability at high temperatures, it can be used to detect reducing gases at 500 °C temperatures and above and to detect oxygen gas [12]. Considering its optical features, it exhibits good photoconductivity under deep UV light due to its wide band gap, making β-Ga_2O_3 suitable for designing devices operating in the UV region [13].

Photodetectors are devices that detect incoming electromagnetic lights and convert them into measurable electrical signals [14]. Here, the detection process is based on the principle of sensing the incoming electromagnetic signal through the photodetector, obtaining an electrical signal at the output, measuring this signal, and detecting the electromagnetic signal [15]. Generally, photodetectors are obtained with semiconductor materials, and they are employed in optical communication, motion detection, night vision systems, and video imaging [16]. Semiconductor photodetectors are generally known as photodiodes and are highly preferred in optical communication systems due to their small size and high detection speed and efficiency [17, 18]. Zhang and his colleagues prepared high-quality β-Ga_2O_3 structures by pulsed laser deposition, and a series of ultraviolet (UV) photodetectors with interdigital electrode structures were prepared by obtaining β-Ga_2O_3 structures with different layer thicknesses [19]. As a result of this study, it was seen that Ga_2O_3 has significant potential in the field of UV detection. In a study conducted by Qin et al. [20], the authors fabricated ultra-high-performance metal–semiconductor-metal (MSM) Schottky barrier photodetectors based on amorphous Ga_2O_3 through a post-annealing process. The obtained results demonstrated the feasibility and practicality of Ga_2O_3 photodetectors for applications in sunblind imaging, environmental monitoring, artificial intelligence and machine vision. A photodetector cell consisting of metal–semiconductor-metal structured Ga_2O_3 photodetector cells was developed by Chen et al. [21]. As a result, it was emphasized that integrating Ga_2O_3-based photodetectors into the array configuration provided a strategy to improve sunblind imaging. Various interlayers can be used for Schottky-type photodetector to improve stability, performance and sensitivity by reducing interface states and controlled trap levels for better operation [22]. Ga_2O_3 can be used in a Schottky-type photodetector for that reasons as interlayer.

Many methods have been used for the deposition of Ga_2O_3 on a surface such as magnetron sputtering [23], spray pyrolysis [24], sol–gel [25], and electrochemical methods [26]. Among these methods, electrodeposition is considered one of the low-cost methods for semiconductor layer fabrication. On the other hand, electrodeposition is a versatile and easy method in which the material can be deposited on the desired conductive substrate under a certain electric field at ambient conditions and room temperature. With this method, the related materials can be coated to the desired extent and thickness by controlling the electric field, pH, and deposition time [27]. The electrochemical coating method has also important advantages such that the layer parameters can be easily controlled and can be applied at room conditions without the need for any complex experimental setup [28]. Consequently, the electrodeposition process is a low-cost, low temperature and scalable alternative to other methods for the growth of Ga_2O_3 thin films [29]. These advantages in material efficiency, eco-friendliness and tunability make them attractive for large area and electronics applications [30].

Ga_2O_3-based photodetectors can be enhanced to detect light over a wide spectrum with their excellent high sensitivity performance [31, 32]. The aim of this study is to combine infrared absorption of Si and UV absorption of Ga_2O_3 to obtain visible light photodetectors. In this work, Ga_2O_3 nanostructures were deposited on an n-Si substrate by electrodeposition technique, and their structural and morphological properties were examined by XRD, SEM and EDX analysis. As a result, grain sizes, surface morphologies, and chemical compositions of Ga_2O_3 nanostructure samples were determined. Afterward, the photodetector structures of Ga_2O_3 samples were designed and fabricated. The characterizations of the fabricated heterojunctions were obtained by *I-V* measurements for various light power illumination intensities and various wavelengths. Thus, photodetector parameters such as responsivity, detectivity, and *EQE* of the Ag/Ga_2O_3/n-Si Schottky photodetector were extracted.

2 Experimental details

An n-type Si wafer was used to fabricate Ag/Ga_2O_3/n-Si Schottky photodetectors. Its carrier concentration, surface resistance, and preferred orientation were 7.3×10^{15} cm^{-3}, 8–10 Ω cm, and (111), respectively. The wafer was sliced into 3 cm × 1 cm pieces, which were cleaned in acetone, deionized water, and isopropanol by an ultrasonic cleaner. Unpolished sides of the pieces were blocked by a tape. Meanwhile, 25 mM Ga_2O_3 powder solution was prepared in HCl and H_2O mixture (2:7), and then the solution was stirred vigorously for one hour. The pH of the solution was adjusted to 6.5 by adding diluted HCl and NH_4OH. In the deposition of Ga_2O_3 nanostructures on the n-Si substrate, same procedures was followed by Ghazalli et al. [33]. The IVIUM VERTEX Potentiostat/Galvanostat device which served as the DC supply unit was employed for the deposition of Ga_2O_3 on n-Si by electrochemical deposition method with a three-electrode at a constant voltage of − 1.7 V for 2 h. At the end of the deposition, the obtained Ga_2O_3 samples were rinsed with distilled water. The nanostructures were put into an oven and annealed at 700 °C for 2 h in the air. A thermal evaporator system was used to obtain Al contacts 150 nm thick on the back and uncoated surfaces. A 100 nm thick Ag metallic contacts, were deposited on the front surfaces of Ga_2O_3/n-Si junction with a hole-array mask of 1 mm diameter or 7.85×10^{-3} cm^2 surface area. Thus, the Ag/Ga_2O_3/n-Si Schottky-type photodetectors were made ready for *I-V* measurements. While the measurement system and schematic diagram of the photodetector is shown in Fig. 1a, optical microscope image and energy band diagram of the photodetector are indicated in Fig. 1b and c, respectively.

ZEISS Supra 40 VP scanning electron microscope (SEM) and energy-dispersive x-ray (EDX) system were used to obtain morphological properties and chemical composition of Ga_2O_3 nanostructures. A Panalytical Empyrean X-ray Diffractometer with CuKα radiation ($\lambda K\alpha = 1542$ Å) was used to detect the crystallographic pattern of Ga_2O_3 nanostructures. DM750 Binocular, fluorescence-capable Microscope was used to obtain optical image of the Ga_2O_3. To collect *I-V* data for various power intensities, the Fytronix FY-7000 solar simulator measurement system was employed, and *I-V* data were obtained for the dark, various light power intensities ranging from 20 to 100 mW/cm^2 in 20 mW/cm^2 intervals. To achieve wavelength-dependent *I-V* characteristics, visible hard-coated bandpass filter kits (Thorlabs GmbH-Germany) were integrated into *I-V* measurement system for 351 nm, 400 nm, 450 nm, 500 nm, 550 nm, 600 nm, 650 nm, 700 nm, 750 nm, and 800 nm wavelength values.

3 Results and discussion

3.1 Structural characterization

XRD is an effective technique for the characterization of crystalline materials since it is harmless to a sample. With this technique, information can be obtained about the crystal orientations (texture) of structures, phases, and other structural parameters such as grain size, crystallinity, strain, and crystal defects [34]. The XRD diffractograms of the Ga_2O_3 nanostructures grown on silicon are shown in Fig. 2a. Characteristic peaks were observed at approximately 28.12°, 30.18°, and 32.45° and no secondary phases can be observed. These peaks are characteristic of the Ga_2O_3 material with monoclinic crystal structure and (400),($\bar{4}$01), and ($\bar{2}$02) orientations (JCPDS Card No: 41-1103) [35].

In addition to determining the phase definition and lattice parameters of the crystalline material, estimation of crystallite size is very important, especially for nanomaterials. Among these, the most commonly used methods are the Scherrer

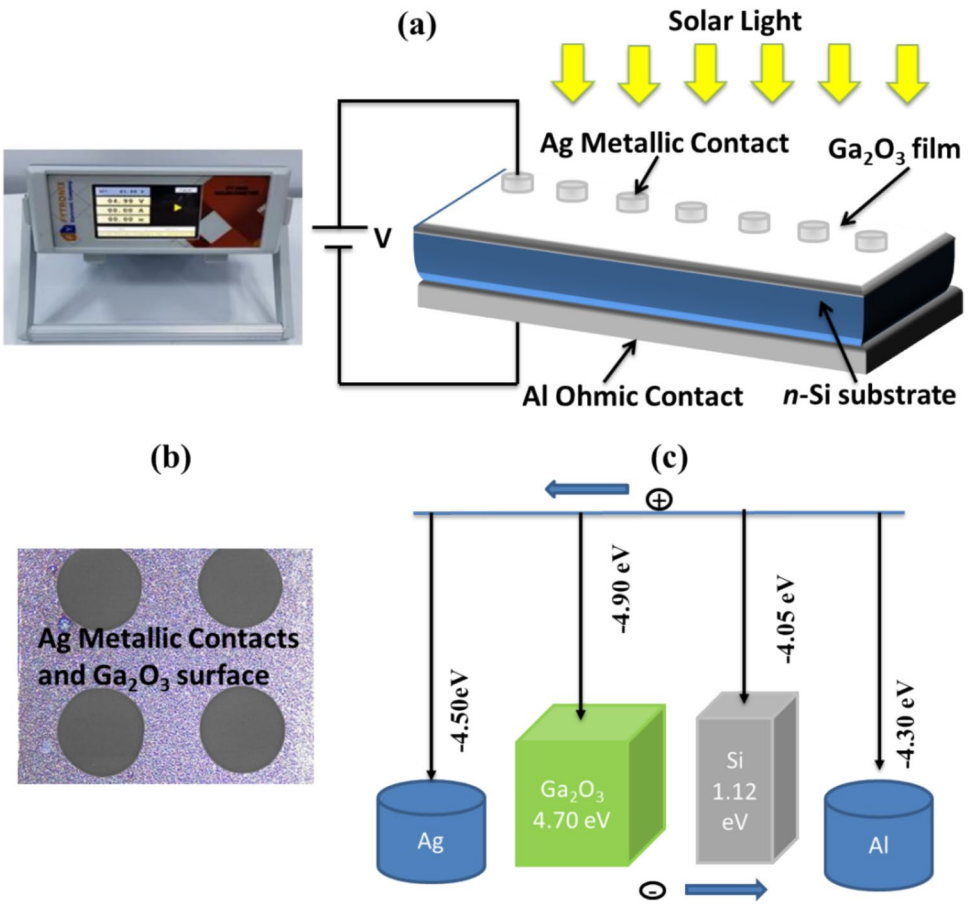

Fig. 1 **a** Schematic diagram and measurement setup, **b** optical microscope image and **c** energy band diagram of the fabricated Ag/Ga_2O_3/n-Si Schottky-type photodetector

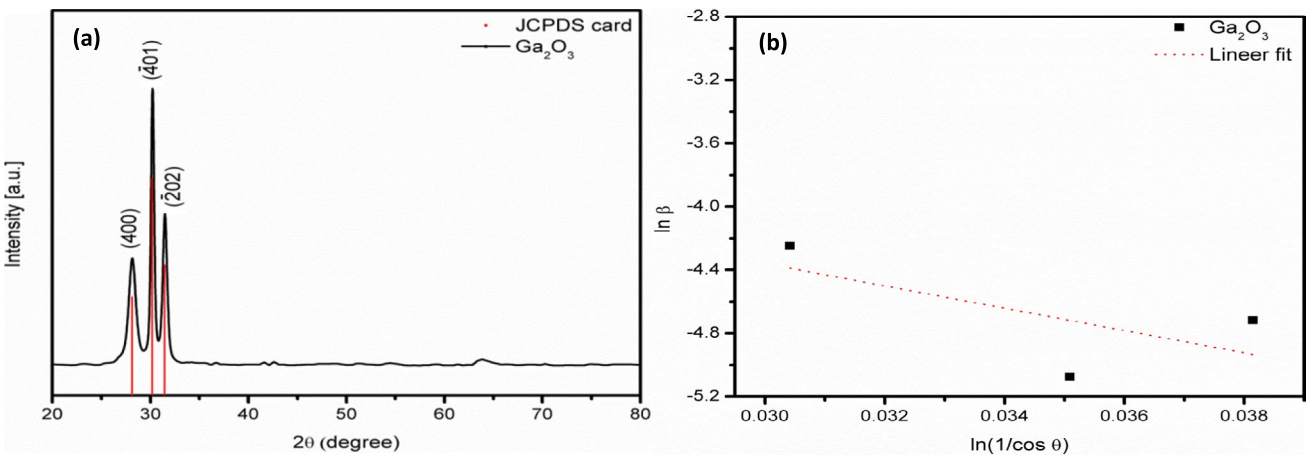

Fig. 2 **a** XRD pattern and **b** modified Scherrer plot of Ga_2O_3 nanostructures

method, Williamson-Hall method, and Halder-Wagner methods. In this study, crystallite size was calculated for Ga_2O_3 nanostructures using these methods. By analyzing the XRD pattern, full with half maximum (FWHM) values were obtained, and using above-mentioned methods, the grain sizes in the planes of the most prominent 2θ peaks were obtained.

The modified Scherrer formula was used to calculate the grain size of the Ga_2O_3 [36]:

$$\ln \beta = \ln \frac{K\lambda}{D} + \ln \frac{1}{\cos\theta}, \quad (1)$$

where D is the particle size of the crystal, K is Scherrer constant to be 0.9, β is the full width at half maximum of the peak, θ is Bragg's diffraction angle and λ is the x-ray wavelength. Although the Scherrer constant (K) was set to 0.9, its exact value for the present material system is not known and therefore crystallite sizes are only estimates. Figure 2b shows the modified Scherrer equation plot from which the average crystallite size can be calculated from the intercept of the fitting line. Using this formula, the structural parameters of the Ga_2O_3 were calculated, as shown in Table 1. Similar results were obtained in a study conducted by Bae et al. [37], who prepared Ga_2O_3 nanostructures by the sol–gel process.

The Williamson-Hall (WH) method is another widely used method to estimate the grain size [38]. Unlike the Scherrer method, it helps to make more comprehensive and accurate calculations by considering internal stresses along with crystal size. The equation derived using $\beta_{hkl} = \beta_{\text{crystallite size}} + \beta_{\text{internal stress}}$ approximation and integral expansion is as follows [39]:

$$\beta\cos\theta = \frac{K\lambda}{D} + 4\varepsilon\sin\theta, \quad (2)$$

where ε indicates internal stresses. Also, the crystallite size may be calculated by the intercept with the horizontal axis of the linear fit [40].

Based on the XRD patterns and using the values calculated by the WH method, $\beta\cos\theta/4\sin\theta$ graphs are drawn in Fig. 3a, and the crystallite dimensions obtained from the graphs are also given in Table 1. In a study reported in the literature [41], the crystallite size values of the β-phase Ga_2O_3 structure synthesized by the hydrothermal method, calculated with the WH technique, are higher than the values we obtained in our study. In many methods, the size expansion of the XRD peak is assumed as a Lorentzian function and the strain expansion is assumed as a Gaussian function. In reality, the XRD peak is neither a Lorentzian nor a Gaussian function. Although the XRD peak region fits the Gaussian function, its tail/branch shows a very rapid decline which does not fit the Gaussian function [42]. To overcome this difficulty, the Halder-Wagner (HW) method, which is the convolution of Gaussian and Lorentzian functions, is used. The advantage of this method is to give more weight to peaks at low and medium angles, where the overlap of diffracting

Table 1 Crystalline size parameters of Ga_2O_3 nanostructures from structural examination by various methods

Sample	(hkl)	d_{hkl} (Å)	2θ (°)	FWHM(°)	D_{SR} (nm)	D_{WH} (nm)	D_{HW}(nm)
Ga_2O_3	(400)	3.1695	28.12	0.8187	16	22	37
	$(\bar{4}01)(\bar{2}02)$	2.9577	30.18	0.3582			
		2.8411	31.45	0.5117			

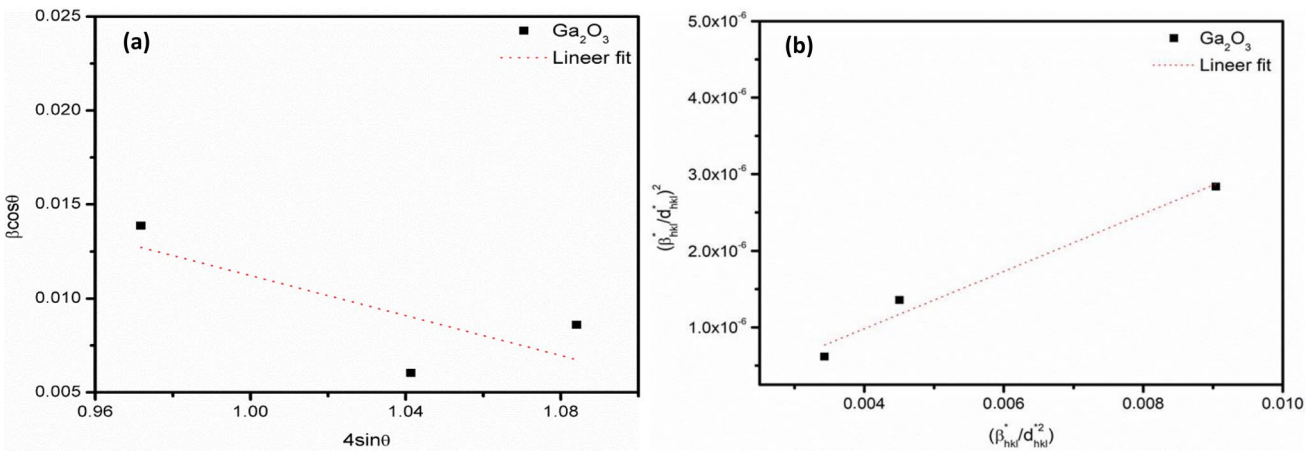

Fig. 3 **a** WH and **b** HW plots of Ga_2O_3 nanostructures

peaks is lower [43]. According to the HW Method, the relationship between crystallite size and internal stresses is given as follows [44]:

$$\left(\frac{\beta^*_{hkl}}{d^*_{hkl}}\right)^2 = \left(\frac{K\lambda}{D}\right)\frac{\beta^*_{hkl}}{d^*_{hkl}} + (4\varepsilon)^2 \quad (3)$$

where $\beta^*_{hkl} = \beta_{hkl}.\cos\theta/\lambda$ and $d^*_{hkl} = 2\sin\theta/\lambda$. With the help of this equation, when the graph is drawn with x-axis $(\frac{\beta^*_{hkl}}{d^{*2}_{hkl}})$ and y-axis $\left(\frac{\beta^*_{hkl}}{d^*_{hkl}}\right)^2$, the slope of the graph gives as a result of linear fit $K\lambda D$ (Fig. 3b). The crystallite dimension obtained by the three above-mentioned methods is reported in Table 1.

3.2 Morphological and elemental characterization

To avoid charging of the Ga_2O_3 surface and obtain better SEM images, the Ga_2O_3 nanostructures were coated with 5 nm thick platinum (Pt) in a vacuum environment by sputtering method. The SEM micrograph of the Ga_2O_3 structures grown on the silicon substrate is shown in Fig. 4a–c for 1 kx, 5 kx, and 30 kx magnifications, respectively. Rod-like structures, with different sizes not distributed homogeneously on the substrate surface can be seen. However, the smallest low resolution Ga_2O_3 nanostructures covered almost the whole surface of Si according to inset of Fig. 4c. The film thickness was determined as around 280 nm. EDX measurement results are shown in Fig. 4d. It should be noted that Si is not taken into account in the weight percentage of the sample since the Ga_2O_3

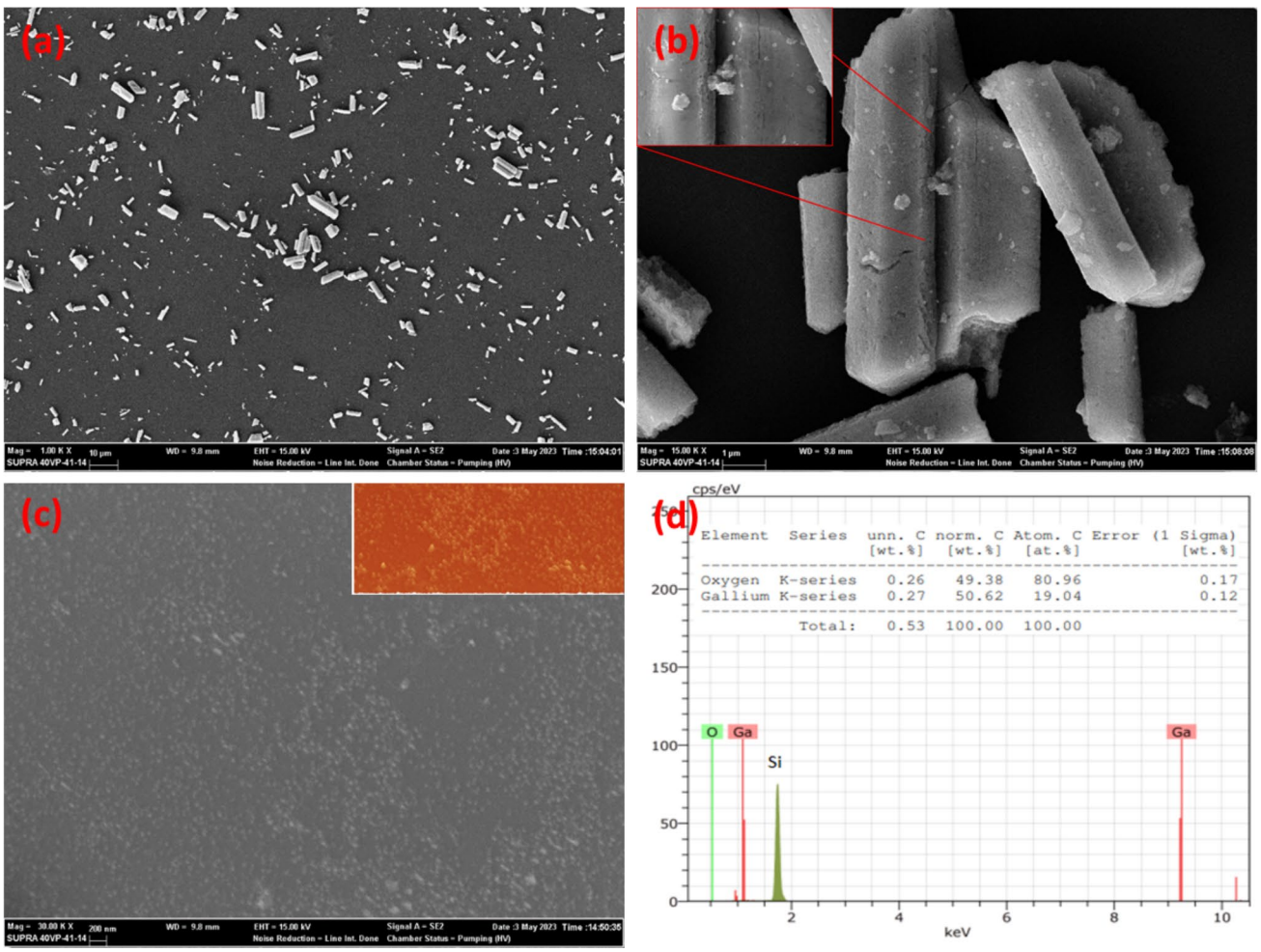

Fig. 4 SEM image of Ga_2O_3 nanostructures grown on the silicon substrate **a** 1 kx **b** 5 kx, **c** 30 kx and **d** EDX spectrum results

nanostructures are coated on the Si base. Ga was found to be 19.22% and O was 80.78% at. These results show the stoichiometric suitability of the sample. The fact that no other elements were found in significant amounts in the nanostructures demonstrates that the purity of them is good.

3.3 Electrical characterizations

I-V characteristics of the Ag/Ga_2O_3/n-Si Schottky-type photodetector and Ag/n-Si heterojunctions for various light power intensities are shown in Fig. 5a and b, respectively. When the light power intensity increased, the current values of the Ag/Ga_2O_3/n-Si and Ag/n-Si Schottky-type photodetector increased due to increasing charge carriers in reverse biases. However, the current values increased for only Ag/Ga_2O_3/n-Si by increasing light power at forward biases. This can be attributed to the fact that Ga_2O_3 layer can increase life time of charge carriers rather than Ag/n-Si Schottky-type photodetector. The increased current at reverse biases confirms the photodetector behavior of the Ag/Ga_2O_3/n-Si and Ag/n-Si Schottky-type photodetectors [45]. To see clearly the increase current at − 2 V, current versus light power density graph has been shown in Fig. 5c and d for both photodetectors. The current increased with increasing light power, confirming the sensitivity of Ag/Ga_2O_3/n-Si to light power changes. However, the current levels of Ag/Ga_2O_3/n-Si are higher than Ag/n-Si due to that Ga_2O_3 improves photodetection with leakage current. Furthermore, the β-phase Ga_2O_3 has n-type conductivity and high electron mobility according to literature due to having oxygen vacancies in the structure [46, 47]. In this study, β-phase Ga_2O_3 was employed as interfacial layer to increase efficiency of the Schottky-type

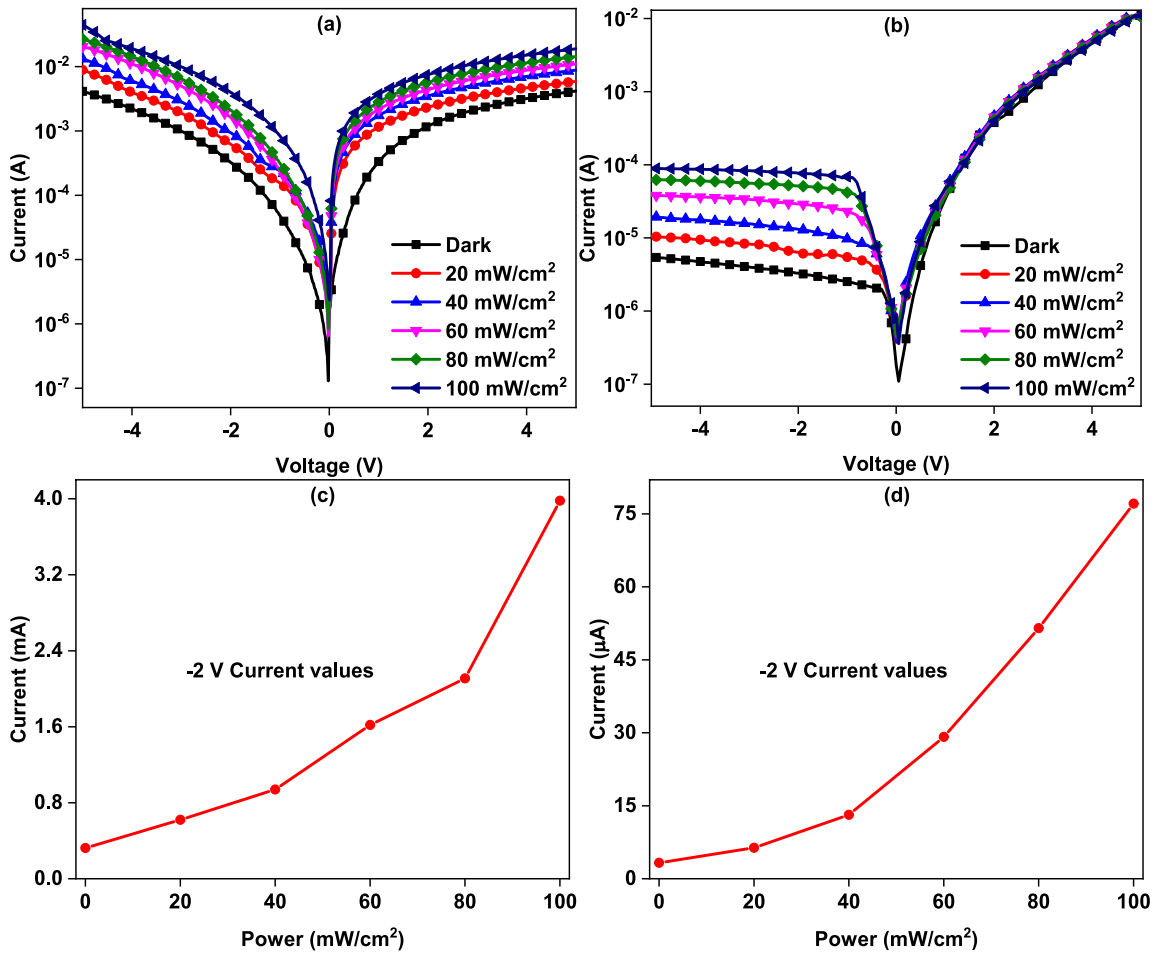

Fig. 5 ln*I-V* plots **a** Ag/Ga_2O_3/n-Si and **b** Ag/n-Si, the current changes at − 2 V biases of **c** Ag/Ga_2O_3/n-Si and **d** Ag/n-Si Schottky-type photodetector depending on light power density

photodetector. The β-phase Ga_2O_3 interlayer may cause to increase electron–hole pairs in the interface of Ag/n-Si or provide to increase transferring of carriers due to its carrier transport layer behavior [48, 49].

Various device parameters such as ideality factor (n), barrier height (Φ_b), etc. can be calculated by thermionic emission theory, Norde, or Cheung methods. Details about these techniques can be found in the literature [50]. The n, Φ_b and saturation current (I_0) values were determined from I-V characteristics by thermionic emission theory for changing light power density, and their values are listed in Table 2. The I_0 values are increased by increasing light power density due to increasing charge carriers. Furthermore, the power-dependent profile of the n and Φ_b have been shown in Fig. 6a. While the n values increased almost linearly by increasing light power density, the Φ_b values decreased due to increasing charge carriers. The increase at the n and the decrease at the Φ_b values by increasing light power density can be ascribed to increasing current levels due to increasing charge carriers by illumination [51, 52]. Another important parameter for metal–semiconductor devices is the junction resistance (R_j) which has two components: series resistance (R_s) for forward biases and shunt resistance (R_{sh}) for reverse biases, and it can be determined by $R_j = dV/dI$ from I-V characteristics data [53]. While the highest value or peak value of the reverse junction resistance shows R_{sh}, the lowest value of the it represent the R_s in forward bias [54]. Figure 6b shows R_j plots of the Ag/Ga_2O_3/n-Si Schottky-type photodetector vs light power density. The R_j values decreased with light power intensity due to increasing charge carrier amounts with light, demonstrating that the Ag/Ga_2O_3/n-Si Schottky-type photodetector has good photoresponse to variation of light power. The determined R_{sh} and R_s values have been listed in Table 2 for changing light power intensity. The given values for R_{sh} and R_s in Table 2 are determined from Fig. 6b for reverse bias around − 0.17 V and forward bias of 4 V, respectively.

Table 2 The device parameters of the Ag/Ga_2O_3/n-Si Schottky-type photodetector depending on intensity of light power density

Light power intensity	Saturation current (I_0)	n (I-V) -	Φ_b(I-V) (eV)	R_{sh} (kΩ)	R_s (kΩ)
Dark (0)	2.73×10^{-6}	2.53	0.62	64.05	1.00
20 mW/cm^2	1.79×10^{-5}	2.61	0.57	35.33	0.85
40 mW/cm^2	2.97×10^{-5}	2.89	0.56	12.92	0.59
60 mW/cm^2	3.65×10^{-5}	3.16	0.56	10.70	0.46
80 mW/cm^2	5.85×10^{-5}	3.44	0.54	9.88	0.35
100 mW/cm^2	9.66×10^{-5}	3.71	0.53	3.96	0.26

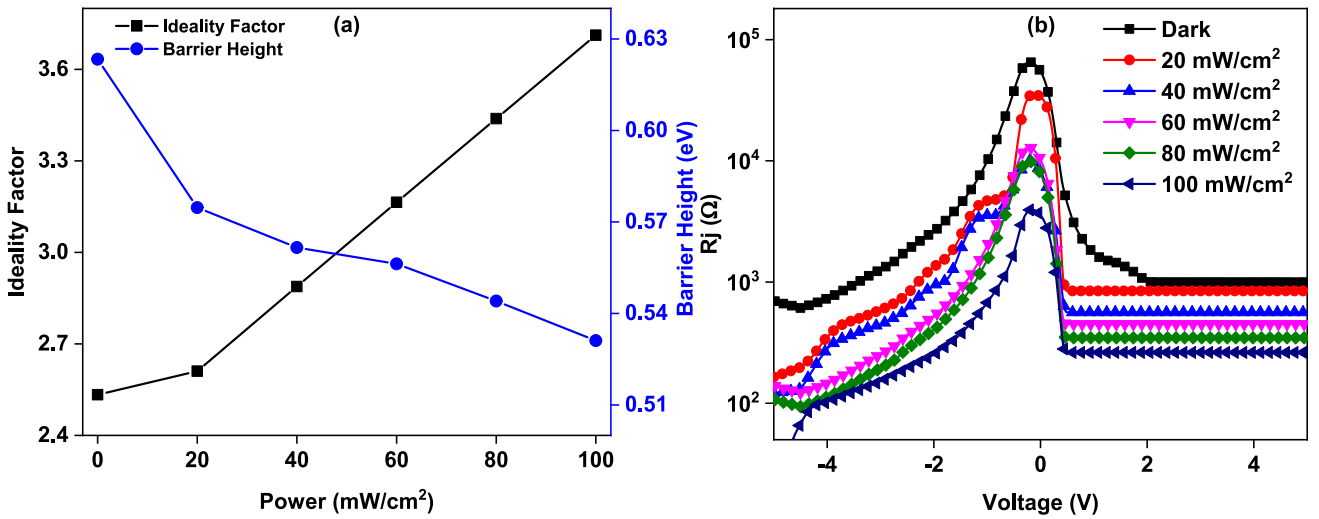

Fig. 6 **a** n an Φ_b d changes, **b** R_j-V plots of Ag/Ga_2O_3/n-Si Schottky-type photodetector for changing light power density

To confirm the consistency of the device parameters, we calculated them by Cheung and Norde methods, separately. The device parameters are calculated using these techniques in literature [55–57]. While the Cheung method proposes two different functions of $H(I)$ and $dV/d(\ln I)$ to determine n, Φ_b, and R_s, the Norde method introduces the Norde function ($F(v)$) to find out Φ_b and R_s values. Cheung and Norde plots of the Ag/Ga_2O_3/n-Si Schottky-type photodetector are shown in Fig. 7a and b, respectively, and the device parameters for the dark condition were calculated for both methods. The Φ_b and R_s values were determined to be 0.62 eV and 3.56 kΩ, respectively, from the Norde method. The n and Φ_b values were obtained as 2.67 and 0.65 eV while the R_s values were figured out to be 1.77 kΩ and 1.81 kΩ by the Cheung method. The parameters obtained by the different methods are in good accordance with each other, apart from small differences that can be attributed to the use of various regions of the I-V characteristics [58].

The key parameters for the detection of light at photodetectors are calculated by following equations of photocurrent (I_p), photosensitivity (K), responsivity (R), and specific detectivity (D^*), respectively:

$$I_p = I_{light} - I_{dark} \tag{4}$$

$$K = \frac{I_p}{I_{dark}} \tag{5}$$

$$R = \frac{I_p}{PA} \tag{6}$$

$$D^* = R\sqrt{\frac{A}{2qI_{dark}}}, \tag{7}$$

where P indicates the power of light and A is the photosensitive area of the photodetector.

Detector parameters of the Ag/Ga_2O_3/n-Si Schottky-type photodetector were determined from the above equations depending on light power density. Figure 8a–d shows photocurrent, responsivity, photosensitivity, and specific detectivity changes of Ag/Ga_2O_3/n-Si Schottky-type photodetector depending on the increasing light power density. Their values have been tabulated in Table 3 for each light power density. Photocurrent changes with increasing light power confirmed the photoconductive behavior of the Ag/Ga_2O_3/n-Si Schottky-type photodetector with an almost linear increase of the current (Fig. 8a). However, excessive photon absorption can lead to local heating, affecting Schottky barrier height and carrier mobility at high optical power densities. The saturation effects can indicate thermal excitation of carriers or nonlinear recombination mechanisms if the device response deviates from linearity at high-power [59]. Slope of the log I_p versus log P was determined as 1.50, which indicates that Ag/Ga_2O_3/n-Si Schottky-type photodetector exhibited unoccupied trap levels [60]. The Ag/Ga_2O_3/n-Si Schottky-type photodetector revealed high responsivity of 4.65 A/W for 100 mW/cm^2, and the responsivity values increased with increasing light power due to fast increase at the photocurrent (Fig. 8b). The photosensivity values also increased linearly with increasing light power density owing to

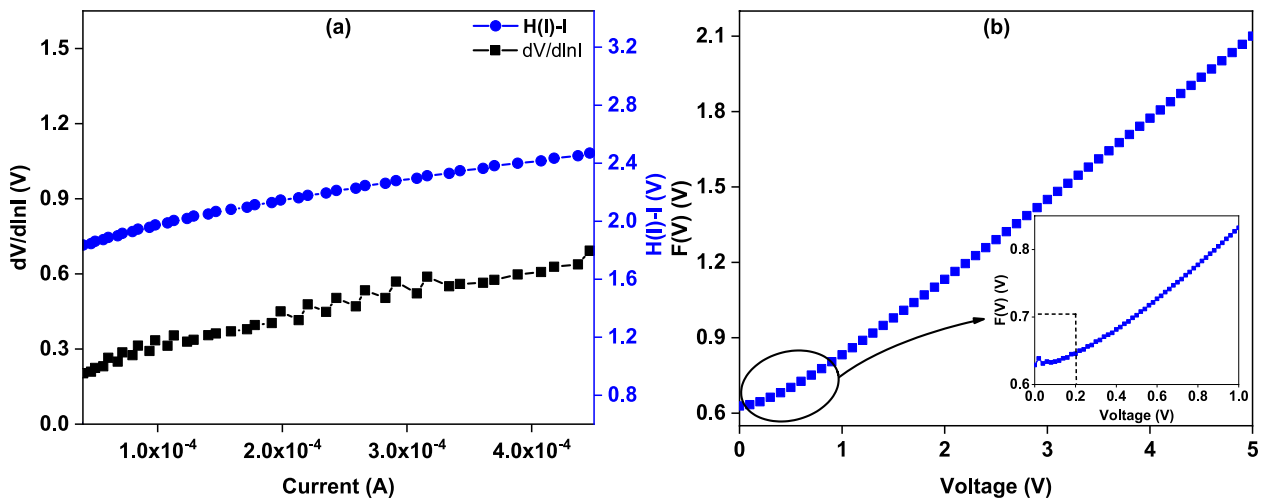

Fig. 7 **a** Cheung functions plots **b** $F(V)$-V plot of the Ag/Ga_2O_3/n-Si Schottky-type photodetector

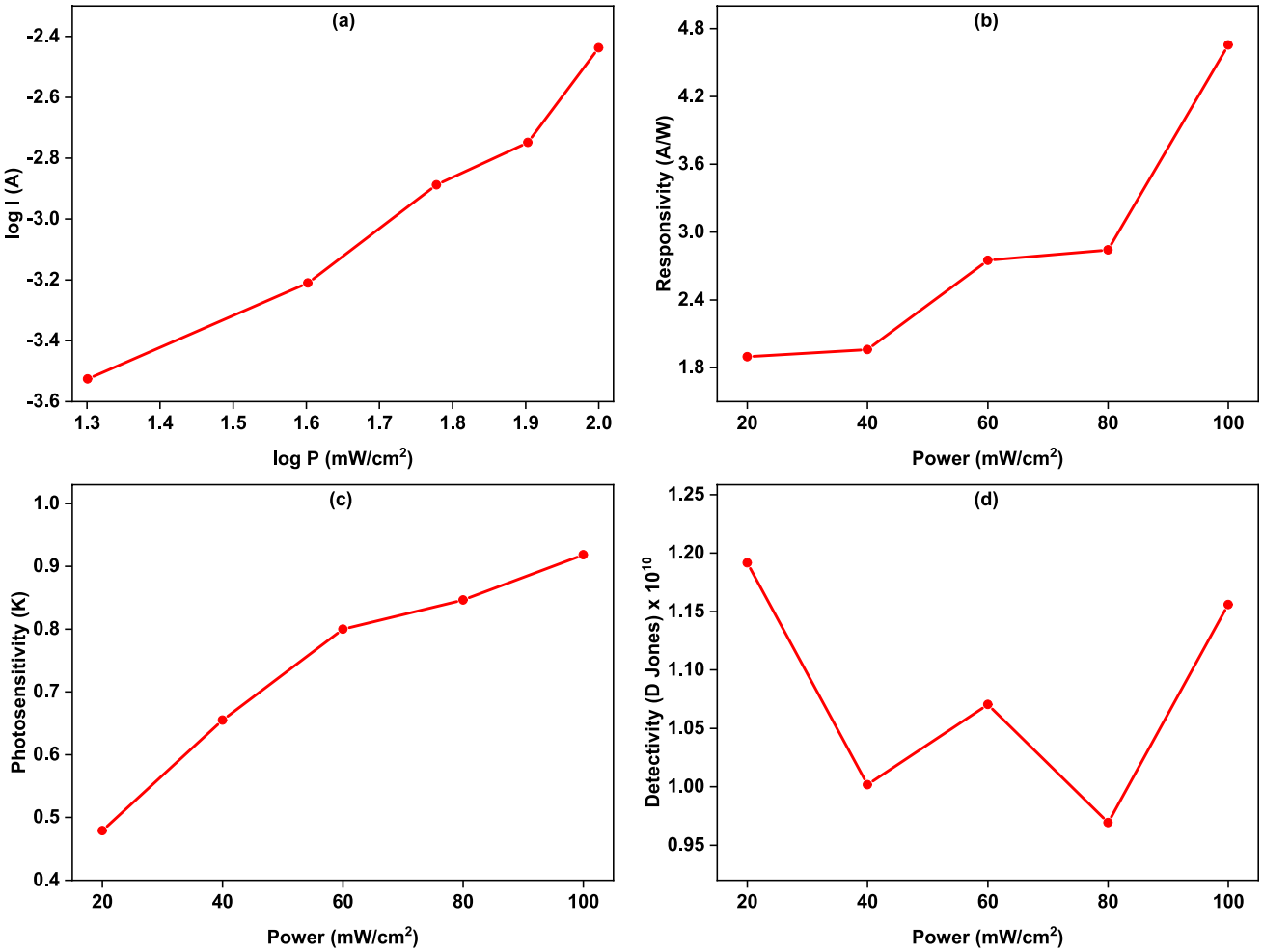

Fig. 8 **a** Logarithmic changes of photocurrent, **b** responsivity, **c** photosensitivity, and **d** detectivity plots of the Ag/Ga_2O_3/n-Si Schottky-type photodetector depending on intensity of light power

good photoconductive behavior of the photodetector (Fig. 8c). The specific detectivity values exhibited fluctuations with changing light power density (Fig. 8d). However, the obtained specific detectivity values are high enough for a Schottky-type photodetector at about 10^{10} Jones levels.

We investigated the performance of the Ag/Ga_2O_3/n-Si Schottky-type photodetector for various wavelengths from 351 to 800 nm by 50 nm intervals. For that reason, *I-V* characteristics of the photodetector were obtained from UV to NIR at 30 mW/cm^2 light power intensity. While Fig. 9a shows *I-V* characteristics, Fig. 9b indicates photocurrent changes for various wavelengths at the same light powers and − 2 V bias. Maximum and minimum photocurrent values were obtained as 4.93×10^{-3} A and 2.41×10^{-2} A at 351 nm and 700 nm, respectively. The Ag/Ga_2O_3/n-Si Schottky-type photodetector shows a good photoresponse to illumination from UV to NIR regions of the electromagnetic spectrum.

Wavelength-dependent profiles of responsivity, photosensitivity, and specific detectivity parameters are shown in Fig. 10a–c, respectively, and their values are reported in Table 3 for various wavelengths. The responsivity values of the Ag/Ga_2O_3/n-Si Schottky-type photodetector increased in visible range and reached 122 A/W at 700 nm (Fig. 10a). The photosensitivity values of the Ag/Ga_2O_3/n-Si photodetector remained almost constant from 400 to 650 nm at around 50 and then reached the maximum value of about 74 at 700 nm (Fig. 10b). The Ag/Ga_2O_3/n-Si Schottky-type photodetector exhibited high detectivity values at around 10^{11} Jones levels, but the maximum value of 1.07×10^{12} Jones was

Table 3 Detector parameters of $Ag/Ga_2O_3/n$-Si Schottky-type photodetector for various power and wavelengths

Conditions	Variations	Photocurrent (A)	Photosensitivity -	Responsivity (A/W)	Specific detectivity (Jones)	*EQE* (%)×10^3
Power (mW/cm^2)	20	2.98×10^{-4}	0.48	1.90	1.19×10^{10}	–
	40	6.16×10^{-4}	0.66	1.96	1.00×10^{10}	–
	60	1.30×10^{-3}	0.80	2.75	1.07×10^{10}	–
	80	1.79×10^{-3}	0.85	2.84	9.69×10^{9}	–
	100	3.66×10^{-3}	0.92	4.65	1.16×10^{10}	–
Wavelength (nm)	351	4.93×10^{-3}	17.33	20.24	1.88×10^{11}	7.17
	400	1.53×10^{-2}	47.31	69.77	6.07×10^{11}	21.63
	450	1.63×10^{-2}	50.34	61.13	5.32×10^{11}	16.84
	500	1.72×10^{-2}	53.08	81.18	7.06×10^{11}	20.13
	550	1.64×10^{-2}	50.71	83.75	7.29×10^{11}	18.88
	600	1.66×10^{-2}	51.08	81.12	7.06×10^{11}	16.76
	650	1.72×10^{-2}	53.08	68.49	5.96×10^{11}	13.07
	700	2.41×10^{-2}	74.40	122.88	1.07×10^{12}	21.77
	750	2.09×10^{-2}	64.53	102.48	8.92×10^{11}	16.94
	800	1.95×10^{-2}	60.21	85.73	7.46×10^{11}	13.29

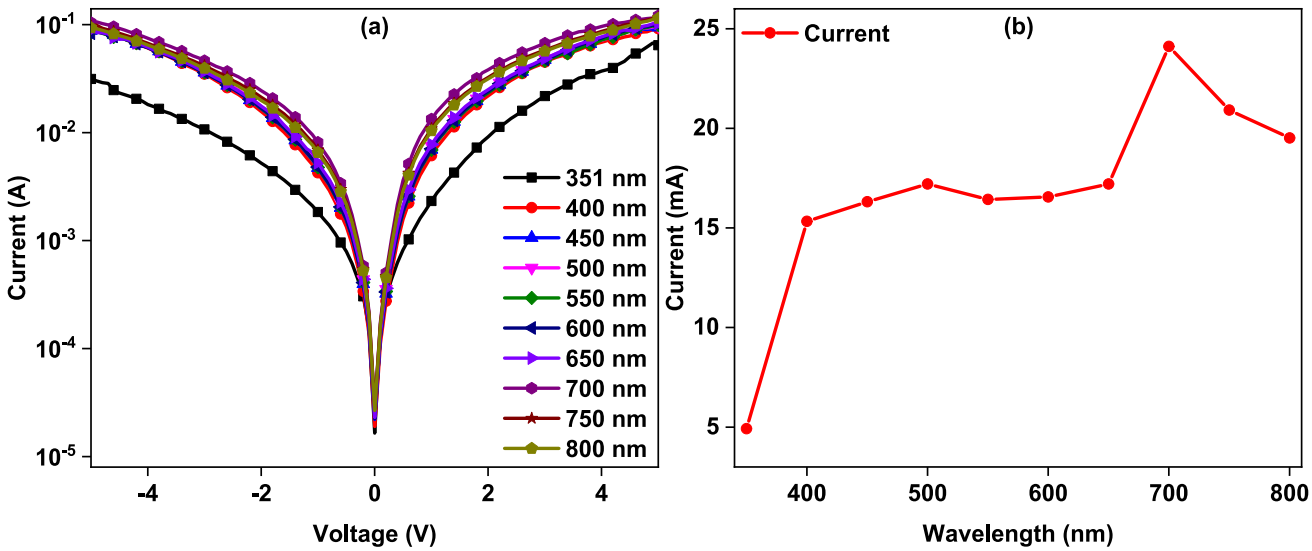

Fig. 9 **a** *I-V* characteristics of the $Ag/Ga_2O_3/n$-Si Schottky-type photodetector at different wavelengths; **b** Photocurrent vs wavelength at − 2 V bias and 30 mW/cm^2 light power

obtained at 700 nm (Fig. 10c). The external quantum efficiency (*EQE*) is a good parameter which defines the performance of the photodetector, and is given by the following equation [61]:

$$EQE = \frac{hc}{e\lambda}R\%\,, \tag{8}$$

where c represents light speed, λ is the incident light wavelength, e indicates the electron charge and h is the Planck constant. The *EQE* profile of the $Ag/Ga_2O_3/n$-Si Schottky-type photodetector is shown in Fig. 10d, and *EQE* values are reported in Table 3 for various wavelengths. The *EQE* values of the $Ag/Ga_2O_3/n$-Si Schottky-type photodetector reached a very high value of 2.18×10^4% at 700 nm.

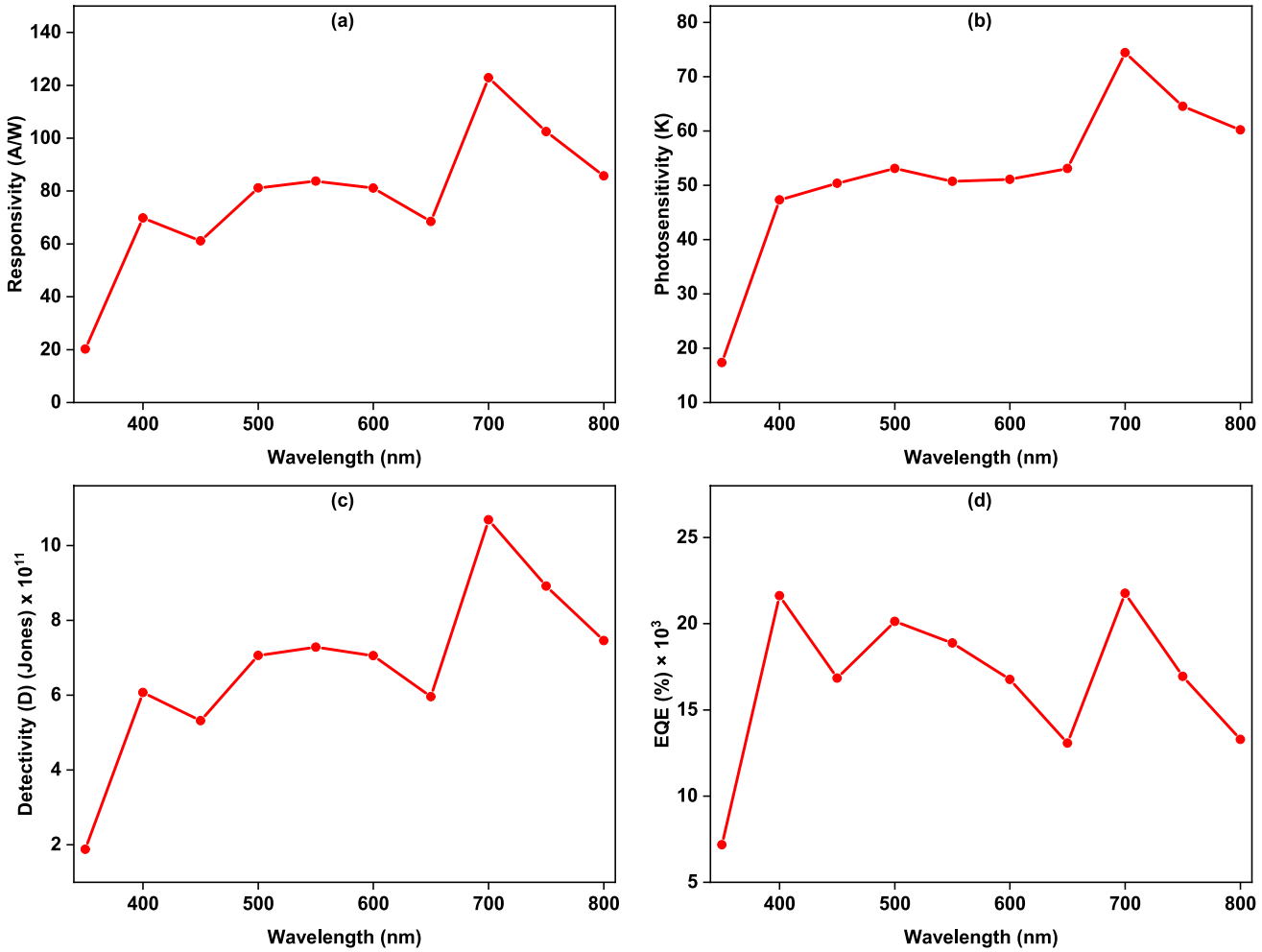

Fig. 10 **a** Responsivity, **b** photosensitivity, **c** detectivity and **d** *EQE* graphs of the Ag/Ga_2O_3/n-Si Schottky-type photodetector for different wavelengths

The performances of the Ag/Ga_2O_3/n-Si Schottky-type photodetector, compared with data reported in the literature were found to be promising, as shown in Table 4. When the literature is surveyed, the fabricated Ag/Ga_2O_3/n-Si has exhibited good performance for photodetector applications.

4 Conclusion

We synthesized Ga_2O_3 nanostructures on n-Si substrates by electrodeposition technique and characterized the structures by XRD, SEM, and EDX analysis. The XRD pattern confirmed the monoclinic crystalline structure of the β-phase Ga_2O_3 nanostructures, and the crystalline size was determined at about 15–40 nm by various methods. While the SEM image revealed rod-like structures on the surface of n-Si, EDX analysis confirmed stoichiometry Ga_2O_3. The Ga_2O_3/n-Si heterostructures were coated with Ag contacts to fabricate Ag/Ga_2O_3/n-Si Schottky-type photodetector. Ag/Ga_2O_3/n-Si was characterized by *I-V* measurements for various light power densities for AM 1.5 sunlight and wavelengths from 351 to 800 nm at 30 mW/cm^2. The device parameters of the Ag/Ga_2O_3/n-Si junction were extracted from *I-V* characteristics using thermionic emission theory, Norde, and Cheung methods. The ideality factor and barrier height values were obtained as 2.53 and 0.62 eV, respectively. The photocurrent, photosensitivity, responsivity, and specific detectivity values were determined for light power density and wavelength changes. The Ag/Ga_2O_3/n-Si Schottky-type

Table 4 $Ag/Ga_2O_3/n$-Si Schottky-type photodetector characteristics compared with data from the literature

Device Structure	Device Type	Wavelength (nm)	Responsivity (A/W)	Detectivity (Jones)	*EQE* (%)	References
Ti/Au/ε-Ga_2O_3/Ti/Au	MSM	254	1.37	9.13×10^{14}	6.67×10^{2}	[62]
Au/Ni/Si-doped β-Ga_2O_3/Ti/Au	MSM	254	366.88	2.33×10^{13}	7.47×10^{4}	[63]
MLG/β-Ga_2O_3/FTO	Schottky diode	230	0.092	5.27×10^{11}	–	[64]
Ti/Au/β-Ga_2O_3/Ti/Au	MSM	254	1.93	6.53×10^{13}	–	[65]
Au/Ti/α-Ga_2O_3/Ti/Au	MSM	254	733	3.90×10^{16}	4.10×10^{5}	[66]
MoS_2/Ga_2O_3	-	900	171	4.60×10^{13}	2.40×10^{4}	[67]
$Ag/Ga_2O_3/n$-Si	Schottky diode	Solar radiation	4.65	1.16×10^{10}	–	This work
$Ag/Ga_2O_3/n$-Si	Schottky diode	700 nm	122.88	1.07×10^{12}	2.18×10^{4}	This work

photodetector has exhibited 122.88 A/W responsivity, 1.07×10^{12} Jones specific detectivity at 700 nm wavelength value. The photodetector exhibited a very high *EQE* value of 2.18×10^{4}% at 700 nm, demonstrating good optoelectronic characteristics from UV to NIR region.

Author contributions

M. Yılmaz: Data curation, writing, reviewing, and editing. A. Kocyigit: Conceptualization, formal analysis, writing—original draft and supervision. E. Erdogan: Conceptualization, formal analysis, writing—original draft. M. Yıldırım: Conceptualization, investigation, and methodology. M. Grilli: Writing—review & editing and supervision.

Funding

Open access funding provided by the Scientific and Technological Research Council of Türkiye (TÜBİTAK). This study was supported by BAP office Bilecik Seyh Edebali University with the grand Number of 2022-01.BŞEÜ.11-01.

Data availability

Data will be ready for authors upon reasonable request.

Declarations

Conflict of interest There is no conflict of interest between authors.

Open Access This article is licensed under a Creative Commons Attribution 4.0 International License, which permits use, sharing, adaptation, distribution and reproduction in any medium or format, as long as you give appropriate credit to the original author(s) and the source, provide a link to the Creative Commons licence, and indicate if changes were made. The images or other third party material in this article are included in the article's Creative Commons licence, unless indicated otherwise in a credit line to the material. If material is not included in the article's Creative Commons licence and your intended use is not permitted by statutory regulation or exceeds the permitted use, you will need to obtain permission directly from the copyright holder. To view a copy of this licence, visit http://creativecommons.org/licenses/by/4.0/.

References

1. I.C. Kizilyalli, O. Blum Spahn, E.P. Carlson, ECS Trans. **109**, 3 (2022)
2. Samriti, V. Rajput, R.K. Gupta, J. Prakash, J. Mater. Chem. C **10**, 73 (2022)
3. T. Mikolajick, G. Galderisi, M. Simon, S. Rai, A. Kumar, A. Heinzig, W.M. Weber, J. Trommer, Solid State Electron. **186**, 108036 (2021)
4. J. Galos, K. Pattarakunnan, A.S. Best, I.L. Kyratzis, C. Wang, A.P. Mouritz, Adv. Mater. Technol. (2021). https://doi.org/10.1002/admt.202001059

5. Z. Li, T. Yan, X. Fang, Nat. Rev. Mater. **8**, 587 (2023)
6. M.V. Nikolic, V. Milovanovic, Z.Z. Vasiljevic, Z. Stamenkovic, Sensors **20**, 6694 (2020)
7. J. Shi, J. Zhang, L. Yang, M. Qu, D. Qi, K.H.L. Zhang, Adv. Mater. (2021). https://doi.org/10.1002/adma.202006230
8. A. Karaca, D.E. Yıldız, A.A. Hussaini, F. Unal, M. Yıldırım, Phys. B Condens. Matter **706**, 417131 (2025)
9. A. Barthel, J. Roberts, M. Napari, M. Frentrup, T. Huq, A. Kovács, R. Oliver, P. Chalker, T. Sajavaara, F. Massabuau, Micromachines **11**, 1128 (2020)
10. H. Zhang, H.-L. Tang, N.-T. He, Z.-C. Zhu, J.-W. Chen, B. Liu, J. Xu, Chin. Phys. B **29**, 087201 (2020)
11. W. Mi, K. Zhang, J. Zhao, Z. Yang, J. Mater. Sci. Mater. Electron. **27**, 11390 (2016)
12. M. Mohamed, I. Unger, C. Janowitz, R. Manzke, Z. Galazka, R. Uecker, R. Fornari, J. Phys. Conf. Ser. **286**, 012027 (2011)
13. H.W. Xue, Q.M. He, G.Z. Jian, S.B. Long, T. Pang, M. Liu, Nanoscale Res. Lett. **13**, 1 (2018)
14. Y. Xu, Q. Lin, Appl. Phys. Rev. **7**, 011315 (2020)
15. H. Ren, J. De Chen, Y.Q. Li, J.X. Tang, Adv. Sci. **8**, 2002418 (2021)
16. N. Nasiri, A. Tricoli, *Industrial applications of nanomaterials* (Elsevier, 2019), pp.123–149
17. R. Hui, *Introduction to fiber-optic communications* (Elsevier, 2020), pp.125–154
18. D.E. Yıldız, H.H. Gullu, M. Yıldırım, N.A. Morley, R. Sahingoz, Nanotechnology **36**, 025203 (2025)
19. X. Zhang, L. Wang, X. Wang, Y. Chen, Q. Shao, G. Wu, X. Wang, T. Lin, H. Shen, J. Wang, X. Meng, J. Chu, Opt. Express **28**, 4169 (2020)
20. Y. Qin, L.-H. Li, Z. Yu, F. Wu, D. Dong, W. Guo, Z. Zhang, J.-H. Yuan, K.-H. Xue, X. Miao, S. Long, Y. Qin, Z. Yu, D. Dong, F. Wu, W. Guo, Z. Zhang, S. Long, L.-H. Li, J.-H. Yuan, K.-H. Xue, X. Miao, Adv. Sci. **8**, 2101106 (2021)
21. Y.-C. Chen, Y.-J. Lu, Q. Liu, C.-N. Lin, J. Guo, J.-H. Zang, Y.-Z. Tian, C.-X. Shan, J. Mater. Chem. C **7**, 2557 (2019)
22. V. Janardhanam, I. Jyothi, M. Zumuukhorol, S.-H. Yuk, K.-H. Shim, C.-J. Choi, Surf. Interfaces **27**, 101405 (2021)
23. A.K. Singh, M. Gupta, V. Sathe, Y.S. Katharria, Superlatt. Microstruct. **156**, 106976 (2021)
24. F.H. Abejide, A.A. Ajayi, S.I. Akinsola, A.B. Alabi, J. Mater. Sci. **57**, 21135 (2022)
25. M.A.A. Hamid, Z. Hassan, S.S. Ng, Int. J. Nanotechnol. **19**, 365 (2022)
26. J.-L. Chiang, B.K. Yadlapalli, M.-I. Chen, D.-S. Wuu, Nanomaterials **12**, 3601 (2022)
27. S. Ruiz-Gómez, C. Fernández-González, L. Perez, Micromachines **13**, 1223 (2022)
28. P.S. Shinde, S. Pan, *Chemical methods processing nanomaterials* (CRC Press, Boca Raton, 2021), pp.59–82
29. N.M. Ghazali, M.R. Mahmood, K. Yasui, A.M. Hashim, Nanoscale Res. Lett. **9**, 120 (2014)
30. L. Tsui, G. Zangari, Electrodepos. Surf. Finish.: Fundam. Appl. (2014). https://doi.org/10.1007/978-1-4939-0289-7_4
31. H. Xu, Y. Weng, K. Chen, C. Wu, H. Hu, D. Guo, Adv. Opt. Mater. (2025). https://doi.org/10.1002/adom.202402238
32. C. Wu, T. Zhao, H. He, H. Hu, Z. Liu, S. Wang, F. Zhang, Q. Wang, A. Liu, F. Wu, D. Guo, Adv. Opt. Mater. (2024). https://doi.org/10.1002/adom.202302294
33. N.M. Ghazali, K. Yasui, A.M. Hashim, Nanoscale Res. Lett. **9**, 685 (2014)
34. A.A. Bunaciu, E. Gabriela Udriştioiu, H.Y. Aboul-Enein, Crit. Rev. Anal. Chem. **45**, 289 (2015)
35. A. Gou, Y. Cheng, F. Zhu, T. Yu, H. Yin, L. Che, J. Chen, X. Zhang, J. Mater. Sci. Mater. Electron. **34**, 1052 (2023)
36. K.M. Wadi, K.A. Jasim, A.H. Shaban, M.K. Kamil, F.K. Nsaif, J. Green Eng. **10**, 6052 (2020)
37. M.-S. Bae, S.-H. Kim, J.-S. Baek, J.-H. Koh, Coatings **11**, 1220 (2021)
38. G.L. Williamson, W. Hall, Acta Metall. **1**, 22 (1953)
39. S.K. Sen, U.C. Barman, M.S. Manir, P. Mondal, S. Dutta, M. Paul, M.A.M. Chowdhury, M.A. Hakim, Adv. Nat. Sci. Nanosci. Nanotechnol. **11**, 025004 (2020)
40. P.M. Kibasomba, S. Dhlamini, M. Maaza, C.-P. Liu, M.M. Rashad, D.A. Rayan, B.W. Mwakikunga, Results Phys. **9**, 628 (2018)
41. R. Pilliadugula, N. Gopalakrishnan, Funct. Mater. Lett. **13**, 2051018 (2020)
42. K. Mouratis, I.V. Tudose, A. Bouranta, C. Pachiu, C. Romanitan, O. Tutunaru, S. Couris, E. Koudoumas, M. Suchea, Nanomaterials **10**, 2397 (2020)
43. S.S. Jahil, I.A. Mohammed, A.R. Khazaal, K.A. Jasim, K.H. Harbbi, NeuroQuantology **20**, 199 (2022)
44. D. Nath, F. Singh, R. Das, Mater. Chem. Phys. **239**, 122021 (2020)
45. P. Ji, S. Yang, Y. Wang, K. Li, Y. Wang, H. Suo, Y.T. Woldu, X. Wang, F. Wang, L. Zhang, Z. Jiang, Microsyst. Nanoeng. **8**, 9 (2022)
46. H. Ma, S. Li, Y. Tong, X. Liu, W. Mu, X. Tao, J. Phys. Chem. C **127**, 6593 (2023)
47. Z. Yang, X. Xu, K.H.L. Zhang, Y. Yang, J. Phys. Chem. Lett. **14**, 4419 (2023)
48. L.-L. Yang, Z. Liu, S. Li, M.-L. Zhang, Z.-Y. Xi, Q. Xu, S.-H. Yan, Y.-F. Guo, W.-H. Tang, IEEE Electron Device Lett. **45**, 420 (2024)
49. M. Labed, B.-I. Park, J. Kim, J.H. Park, J.Y. Min, H.J. Hwang, J. Kim, Y.S. Rim, ACS Nano **18**, 6558 (2024)

50. O.S. Cifci, M. Bakir, J.L. Meyer, A. Kocyigit, Mater. Sci. Semicond. Process. **74**, 175 (2018)
51. D.R. Lambada, S. Yang, Y. Wang, P. Ji, S. Shafique, F. Wang, Nanomanuf. Metrol. **3**, 269 (2020)
52. H.E. Lapa, A. Kökce, D.A. Aldemir, A.F. Özdemir, J. Mater. Sci. Mater. Electron. **32**, 4448 (2021)
53. L.D. Rao, V.R. Reddy, in *AIP Conf. Proc.* (AIP Publishing LLC, 2016), p. 120020.
54. C.V. Prasad, J.H. Park, J.Y. Min, W. Song, M. Labed, Y. Jung, S. Kyoung, S. Kim, N. Sengouga, Y.S. Rim, Mater. Today Phys. **30**, 100932 (2023)
55. S.K. Cheung, N.W. Cheung, Appl. Phys. Lett. **49**, 85 (1986)
56. M. Yilmaz, A. Kocyigit, B.B. Cirak, H. Kacus, U. Incekara, S. Aydogan, Mater. Sci. Semicond. Process. **113**, 105039 (2020)
57. H. Norde, J. Appl. Phys. **50**, 5052 (1979)
58. A. Kocyigit, M. Yılmaz, Ş Aydoğan, Ü. İncekara, J. Alloys Compd. **790**, 388 (2019)
59. J. Tian, L. Chen, R. Qiao, K. Xiong, W. Zhang, Y. Mao, H. Li, J. Li, Nano Energy **79**, 105435 (2021)
60. M. Yıldırım, J. Alloys Compd. **773**, 890 (2019)
61. B. Ezhilmaran, A. Patra, S. Benny, M.R. Sreelakshmi, V.V. Akshay, S.V. Bhat, C.S. Rout, J. Mater. Chem. C **9**, 6122 (2021)
62. S. Li, J. Yue, X. Ji, C. Lu, Z. Yan, P. Li, D. Guo, Z. Wu, W. Tang, J. Mater. Chem. C **9**, 5437 (2021)
63. W.Y. Jiang, Z. Liu, S. Li, Z.Y. Yan, C.L. Lu, P.G. Li, Y.F. Guo, W.H. Tang, IEEE Sens. J. **21**, 18663 (2021)
64. Y. Li, Z. Zhou, H. Pan, J. Chen, Y. Wang, Q. Qu, D. Zhang, M. Li, Y. Lu, Y. He, J. Mater. Res. Technol. **22**, 2174 (2023)
65. S. Zhou, X. Peng, H. Liu, Z. Zhang, L. Ye, H. Li, Y. Xiong, L. Niu, F. Chen, L. Fang, C. Kong, W. Li, X. Yang, H. Zhang, Opt. Mater. Express **12**, 327 (2022)
66. Y. Qin, L. Li, Z. Yu, F. Wu, D. Dong, W. Guo, Z. Zhang, J. Yuan, K. Xue, X. Miao, S. Long, Adv. Sci. (2021). https://doi.org/10.1002/advs.202101106
67. R. Wadhwa, D. Kaur, Y. Zhang, A. Alexender, D. Kumar, P. Kumar, M.A.G. Namboothiry, Q. Qiao, M. Kumar, Appl. Surf. Sci. **632**, 157597 (2023)

Publisher's Note Springer Nature remains neutral with regard to jurisdictional claims in published maps and institutional affiliations.